Supplement of Atmos. Meas. Tech., 19, 7231–7254, 2026
https://doi.org/10.5194/amt-19-7231-2026-supplement
© Author(s) 2026. CC BY 4.0 License.



Atmospheric Measurement Techniques
Open Access
EGU

Supplement of

Two decades of kilometer-scale daily $PM_{2.5}$ from satellite observations and machine learning reveal geographically diverging exposure in Ghana

Abhishek Anand et al.

Correspondence to: Abhishek Anand (abhishek.anand@columbia.edu)

The copyright of individual parts of the supplement might differ from the article licence.

Table S1. Technical specifications of particulate monitors deployed in Ghana.

Sensor type	**Relevant measurement variables**	**Measurement frequency**	**Operating $PM_{2.5}$ range ($\mu g\ m^{-3}$)**
Airnote v2.0	$PM_{2.5}$, T, RH	1 min	0–1000
BAM	$PM_{2.5}$, T, RH	1 hr	0–10,000
Clarity Node-S (Generation II)	$PM_{2.5}$, T, RH	1 min	0–1000
PA-II SD	$PM_{2.5}$, T, RH	2 min	0–1000
MODULAIR-PM	$PM_{2.5}$, T, RH	1 min	0–2000

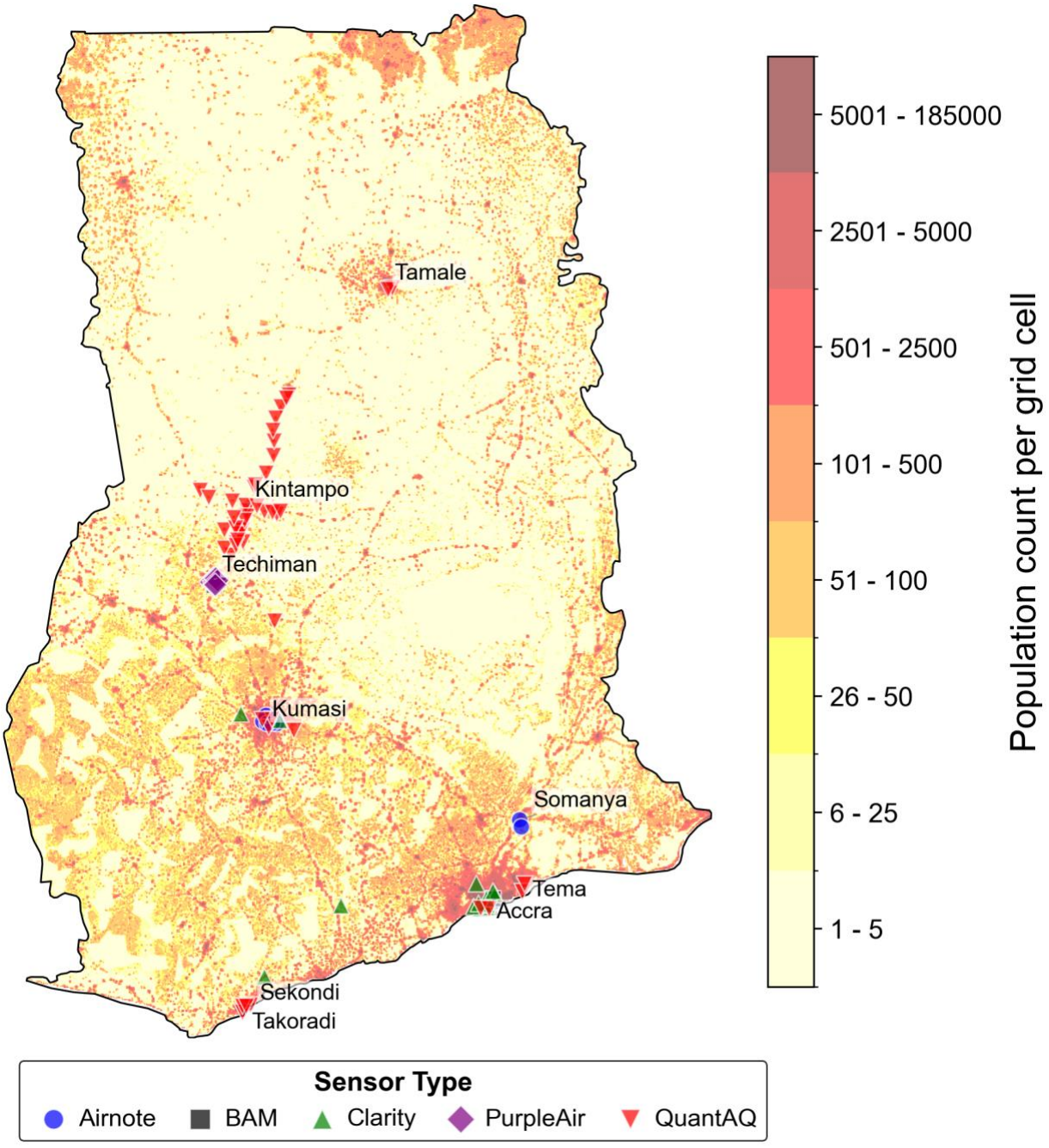


Fig. S1. Map of sensor locations. A map of Ghana showing the locations and counts of all surface $PM_{2.5}$ monitors and the population density for 2024 from the LandScan Program at Oak Ridge National Lab (Lebakula et al., 2024). The darker regions indicate higher population density.

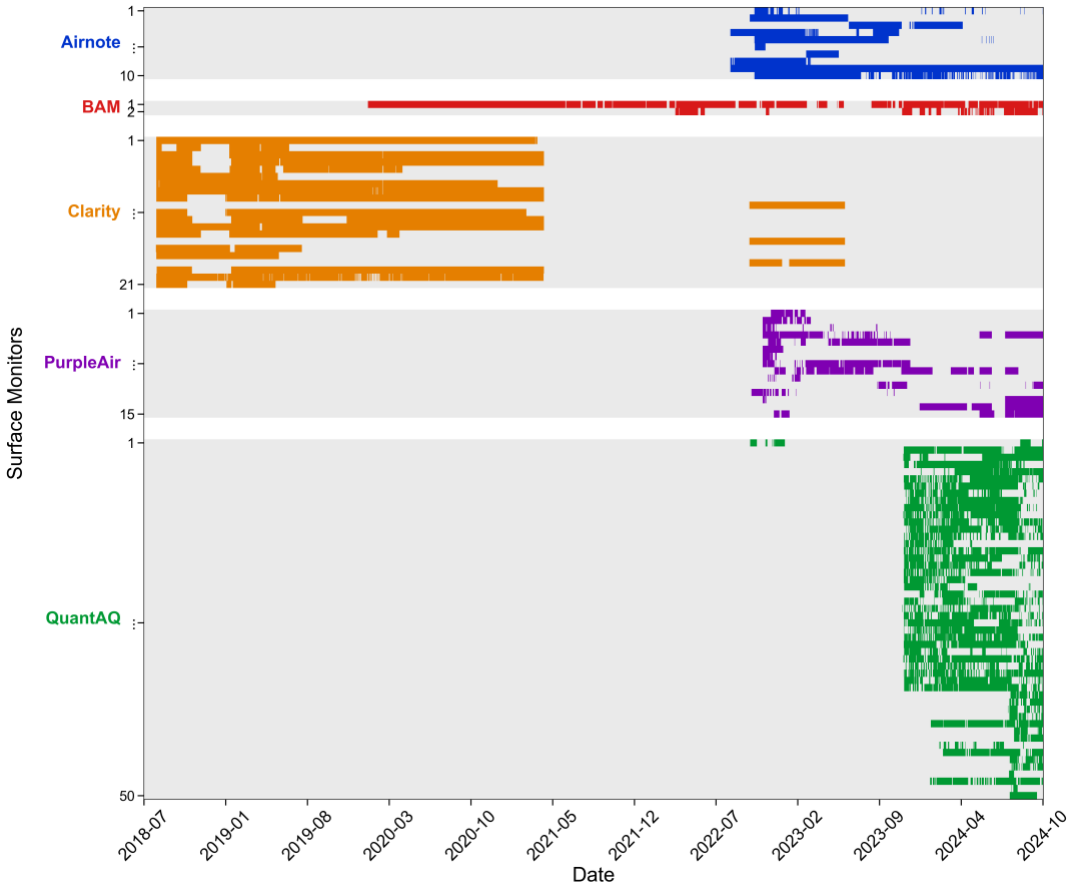


Fig. S2. Availability of $PM_{2.5}$ measurements from 98 surface monitors used as ground truth for building the model. Y-axis represents different sensor types and their corresponding numbers.

Table S2. Summary of sensor locations, location types and corresponding counts in Ghana.

Location	**Site classification**	**Sensor count**
Accra	Urban	20
Kintampo	Rural/peri-urban	35
Kumasi	Urban	13
Nyamibechire	Peri-urban	1
Sekondi	Urban	1
Somanya	Peri-urban	3
Supomu Dunkwa	Peri-urban	1
Takoradi	Urban	3
Tamale	Urban	3
Techiman	Peri-urban	16
Tema	Urban	2

Table S3. Summary of total and location-aggregated counts for each sensor types used in Ghana.

Sensor types	**Count**	**Locations**
Airnote	10	Kumasi (7) Somanya (3)
BAM	2	Accra (1) Techiman (1)
Clarity	21	Accra (17) Kumasi (2) Nyamibechire (1) Supomu Dunkwa (1)
PurpleAir	15	Techiman (15)
QuantAQ	50	Accra (2) Kintampo (35) Kumasi (4) Sekondi (1) Takoradi (3) Tamale (3) Tema (2)

Text S1. Calibration of $PM_{2.5}$ measurements from low-cost sensors

Each of the low-cost sensors (Airnote, Clarity, PurpleAir and QuantAQ) in the surface monitoring network was calibrated collocating either with a BAM or other BAM-corrected low-cost monitors in the network. The corrected $PM_{2.5}$ concentrations were calculated using the equation below.

$$PM_{2.5,\ corrected} = f(PM_{2.5,\ raw}, T, RH) \ldots (S1)$$

where $PM_{2.5,\ raw}$, T and RH denote raw measurements of $PM_{2.5}$, temperature (in ºC) and relative humidity (in %) collected by a low-cost sensor. $PM_{2.5,\ corrected}$ represents the quality-assured/quality-controlled (QA/QC) $PM_{2.5}$ concentrations retrieved from calibration algorithms.

Airnote

Airnote sensors were mainly deployed in Kumasi (urban) and Somanya (peri-urban). Following the calibration procedure described by Owusu-Tawiah et al. (2025), we developed a multiple linear regression (MLR) model using measurements collected between September and December 2023 from Airnotes collocated with a Teledyne T640 reference monitor. Airnote-measured $PM_{2.5}$, temperature, and relative humidity (RH) were used as predictor variables, while $PM_{2.5}$ measurements from the T640 were used as the response variable. The resulting equation was:

$$PM_{2.5,\ corrected} = -6.6 + 0.57*PM_{2.5,\ raw} + 0.28*T + 0.03*RH \ldots (S2)$$

Clarity

The majority of Clarity sensors are located in Accra and a few in Kumasi, Supomu Dunkwa and Nyamibechire. An MLR algorithm was developed using BAM located at Accra US Embassy as reference monitor (Raheja et al., 2023).

$$PM_{2.5,\ corrected} = 54.60 + 0.4*PM_{2.5,\ raw} - 0.76*T - 0.35*RH \ldots (S3)$$

PurpleAir

All PA-II SD sensors were deployed in Techiman. Each PurpleAir sensor consists of two identical Laser Particle Counters (PMS-5003, PlanTower, Beijing, China) to measure $PM_{2.5}$, named channel A and B. A BME280 sensor (Bosch, Gerlingen, Germany) measures pressure, temperature and humidity sensor which can be used for calibrating the raw $PM_{2.5}$ measurements. We applied three filtering criteria to include only valid data points in the analysis: (1) a $PM_{2.5}$ threshold for both channels to 1000 µg m^{-3} and discarded datapoints with $PM_{2.5}$ higher than the threshold to comply

with the manufacturer recommendation, (2) keep only rows with valid entry in temperature, humidity and $PM_{2.5}$ concentrations from the two channels, and (3) retains rows where relative percentage difference in $PM_{2.5}$, defined as $2*100*|PM_{2.5,A} - PM_{2.5,B}|/(PM_{2.5,A} + PM_{2.5,B})$, is $\leq$ 25%, which neglects datapoints with large differences in $PM_{2.5}$ readings from the two channels mostly attributed to ageing of either or both laser particle counters or their clogging due to accumulation of dust or insects.

The $PM_{2.5}$ measurements from Techiman BAM were used as ground-truth for calibrating PurpleAir-based $PM_{2.5}$ concentrations. A PurpleAir sensor within the Techiman network located at ~500m to the BAM was selected for model development due to its closest proximity to the BAM. An eXtreme Gradient Boosting (XGBoost) model was developed to derive corrected $PM_{2.5}$.

$$PM_{2.5,\,XGBoost\text{-}corrected} = f(\text{Mean } PM_{2.5,\,raw}, T, RH) \quad \ldots(S4)$$

where, Mean $PM_{2.5,\,raw}$ is the average of raw $PM_{2.5}$ measurements from channels A and B. $PM_{2.5,XGBoost\text{-}corrected}$ represents model corrected $PM_{2.5}$. This model is further used to correct $PM_{2.5}$ outputs from the rest of the PurpleAir sensors in the Techiman network.

QuantAQ

MODULAIR-PM reports $PM_{2.5}$ after applying manufacturer-built correction that accounts for particle density, aspiration efficiency, and hygroscopic growth. These measurements have shown strong correlation with reference measurements and were comparable to corrected $PM_{2.5}$ from regression and machine learning algorithms developed for operation in specific environments (Raheja et al., 2023). Therefore, the $PM_{2.5}$ measurements reported by the MODULAIR monitors in the network were directly used for model development.

Table S4. Quality screening of satellite-derived products. A summary of satellite-derived products and corresponding QA criteria to generate high-quality retrievals.

Parameters	**Satellite product (*ID*)**	**QA layers and criteria**
AOD at 550 nm (MODIS MAIAC)	AOD (*MCD19A2*)	*AOD_QA* ϵ {0000, 0011, 1011} (*AOD_QA* is a 16-bit unsigned integer.)
OMI (Level 2, Collection 3)	UVAI (*OMAERUV v003*)	*CloudFraction* ≤ 0.3 *SolarZenithAngle* ≤ 75º *XTrackQualityFlags* = 0
	HCHO (*OMHCHO v003*)	*AMFCloudFraction* ≤ 0.3 *SolarZenithAngle* ≤ 75º *XTrackQualityFlags* = 0 *MainDataQualityFlag* = 0
	O_3 (*OMTO3 v003*)	*RadiativeCloudFraction* ≤ 0.3 *SolarZenithAngle* ≤ 85º *QualityFlags* ≤ 1
	NO_2 (*OMNO2 v003*)	*CloudFraction* ≤ 0.3 *SolarZenithAngle* ≤ 75º *VcdQualityFlags* = 0
	SO_2 (*OMSO2 v003*)	*CloudRadiationFraction* ≤ 0.3 *SolarZenithAngle* ≤ 65º *Flag_RowAnomaly* ≠ 1 *Flag_SAA* ≠ 1 *AlgorithmFlag_SnowIce* ≠ 2
TROPOMI (Level 2, Collection 2)	UVAI *(S5P_L2__AER_AI_HiR v2)*	*qa_value* ≥ 0.5
	HCHO *(S5P_L2__HCHO___HiR v2)*	
	O_3 *(S5P_L2__O3_TOT_HiR v2)*	
	NO_2 *(S5P_L2__NO2____HiR v2)*	
	SO_2 *(S5P_L2__SO2____HiR v2)*	

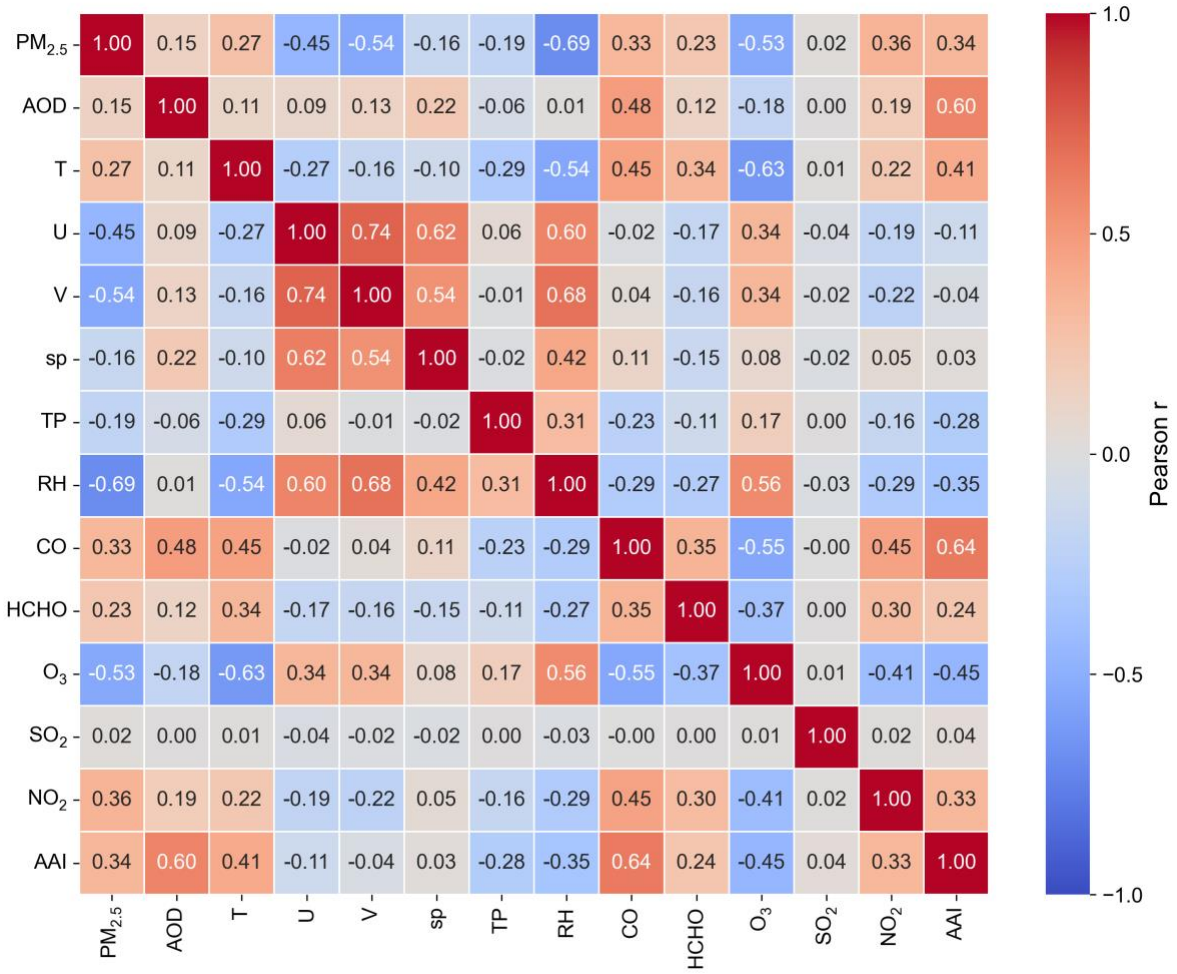


Fig. S3. Correlation between training features used in TROPOMI model. Pearson correlation matrix of $PM_{2.5}$, meteorological (ERA5), and satellite-derived (MODIS and TROPOMI) variables used in the modeling framework. Color intensity represents the strength and direction of linear correlations, ranging from −1 (strong negative correlation) to +1 (strong positive correlation).

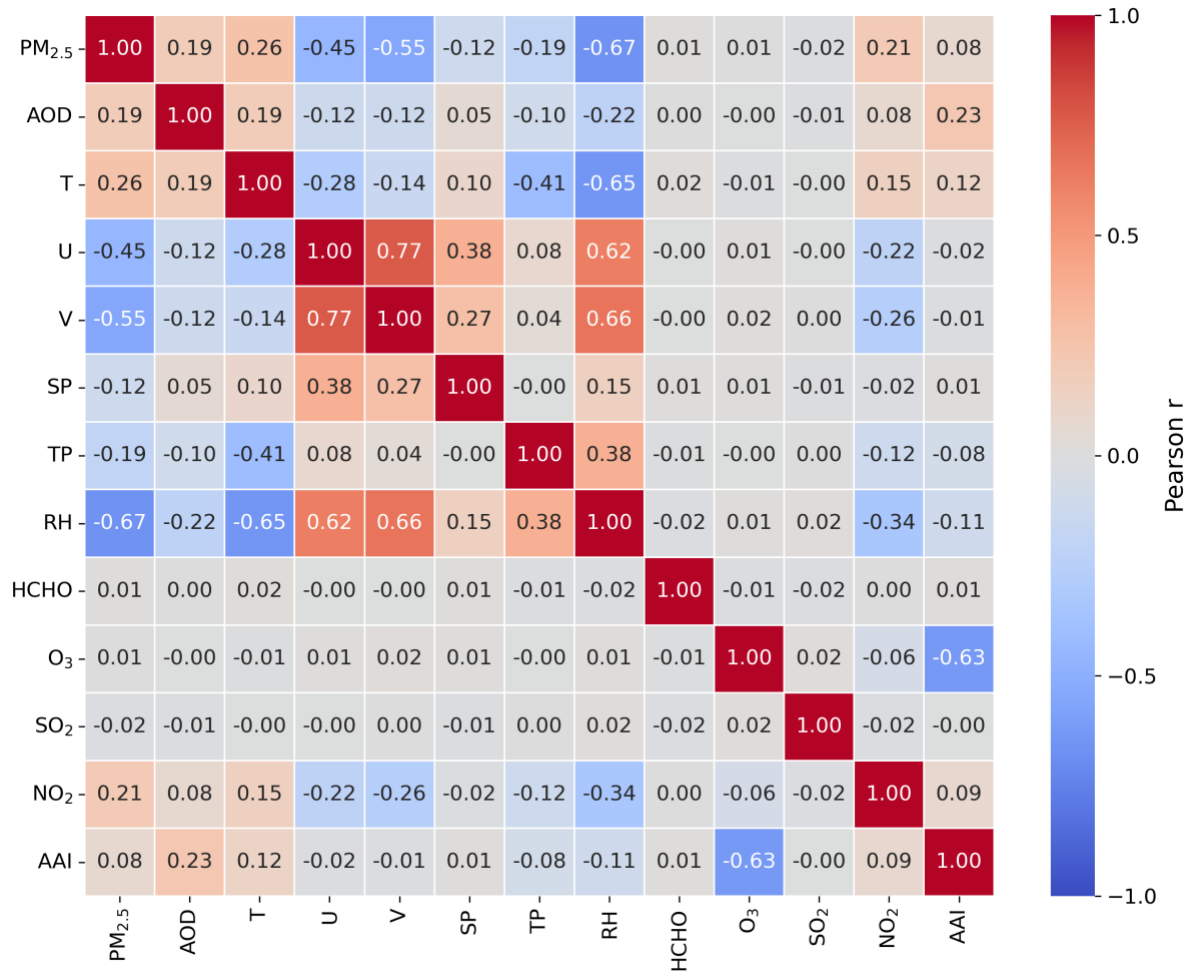


Fig. S4. Correlation between training features used in OMI model. Pearson correlation matrix of $PM_{2.5}$, meteorological (ERA5), and satellite-derived (MODIS and OMI) variables used in the modeling framework. Color intensity represents the strength and direction of linear correlations, ranging from −1 (strong negative correlation) to +1 (strong positive correlation).

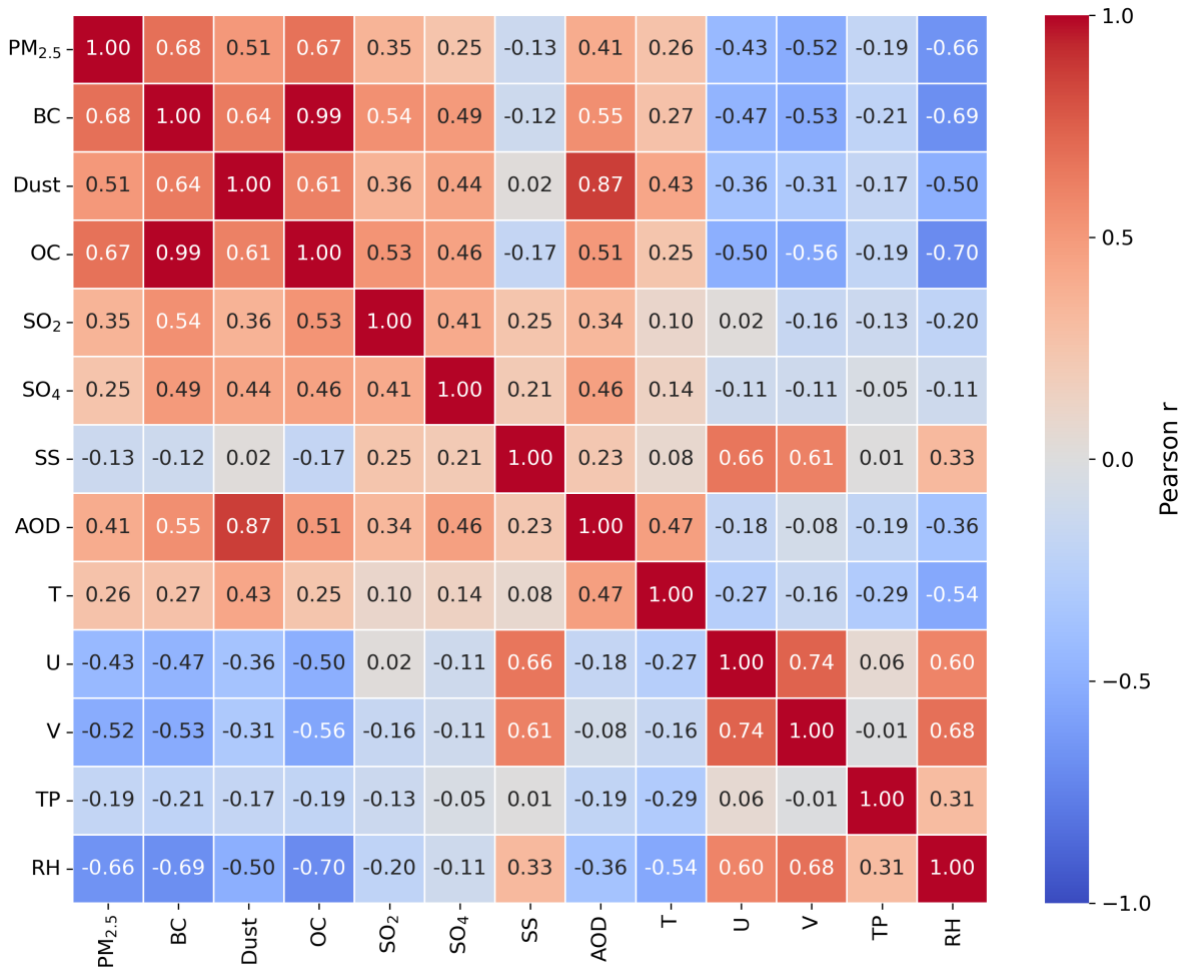


Fig. S5. Correlation between training features used in MERRA2-based model. Pearson correlation matrix of $PM_{2.5}$, meteorological (ERA5), and MERRA-2 reanalysis variables used in the modeling framework. Color intensity represents the strength and direction of linear correlations, ranging from −1 (strong negative correlation) to +1 (strong positive correlation).

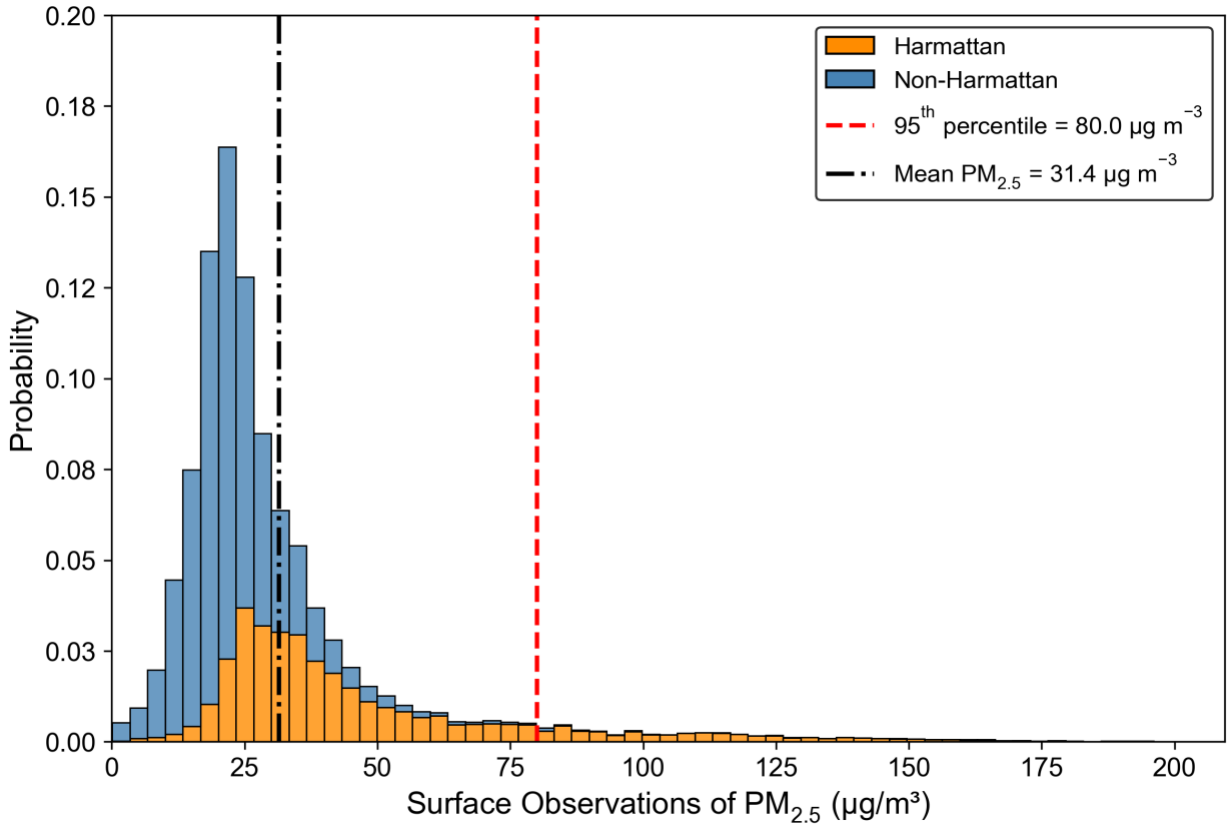


Fig. S6. Surface $PM_{2.5}$ measurements from ground monitors. Probability distribution of surface-observed $PM_{2.5}$ concentrations (µg m^{-3}) stratified into Harmattan (orange) and non-Harmattan (blue) periods. The histogram represents the relative frequency of observations, where the red dashed vertical line indicates the 95th percentile (80 µg m^{-3}) and black dash-dotted line denotes the mean concentration (31.4 µg m^{-3}). The distribution is positively skewed, with most observations concentrated at lower concentrations and a long tail toward higher pollution events.

Text S2. Selection of $PM_{2.5}$ grid cells for urban locations

To obtain a representative $PM_{2.5}$ time series for each of the 20 study locations, 1-km $PM_{2.5}$ grid cells representing each location were identified based on the spatial extent and morphology of the built-up area. Where available, the Global Human Settlement Layer Urban Centre Database (GHS-UCDB) (Melchiorri et al., 2024) was used as the primary spatial reference for characterizing the spatial extent of each urban center. The GHS-UCDB urban-center boundaries, 1-km $PM_{2.5}$ grid, and city reference locations were overlaid to assess the spatial correspondence between the urban centers and the $PM_{2.5}$ grid.

For locations with a corresponding GHS-UCDB urban center, grid cells intersecting the GHS-UCDB urban-center boundary were used as the core set of cells. Adjacent grid cells were subsequently evaluated based on the continuity of built-up development and the surrounding spatial context to identify cells representing the broader area associated with each study location. Cells were included when they represented a contiguous extension of the built-up area associated with the study location, whereas cells separated from the developed area by clearly undeveloped or predominantly rural land, or containing isolated development, were excluded (Fig. S7). For locations without a dedicated GHS-UCDB urban-center boundary (Accra, Damongo, Goaso, Nalerigu, Navrongo, Sefwi Wiawso, and Tema), the city reference location and surrounding built-up morphology were used to identify representative grid cells using the same criteria.

This approach allowed the spatial extent of the selected $PM_{2.5}$ grid cells to vary according to the size and morphology of the built-up area surrounding each study location. The final selected grid cells were used to calculate the representative $PM_{2.5}$ time series for each location.

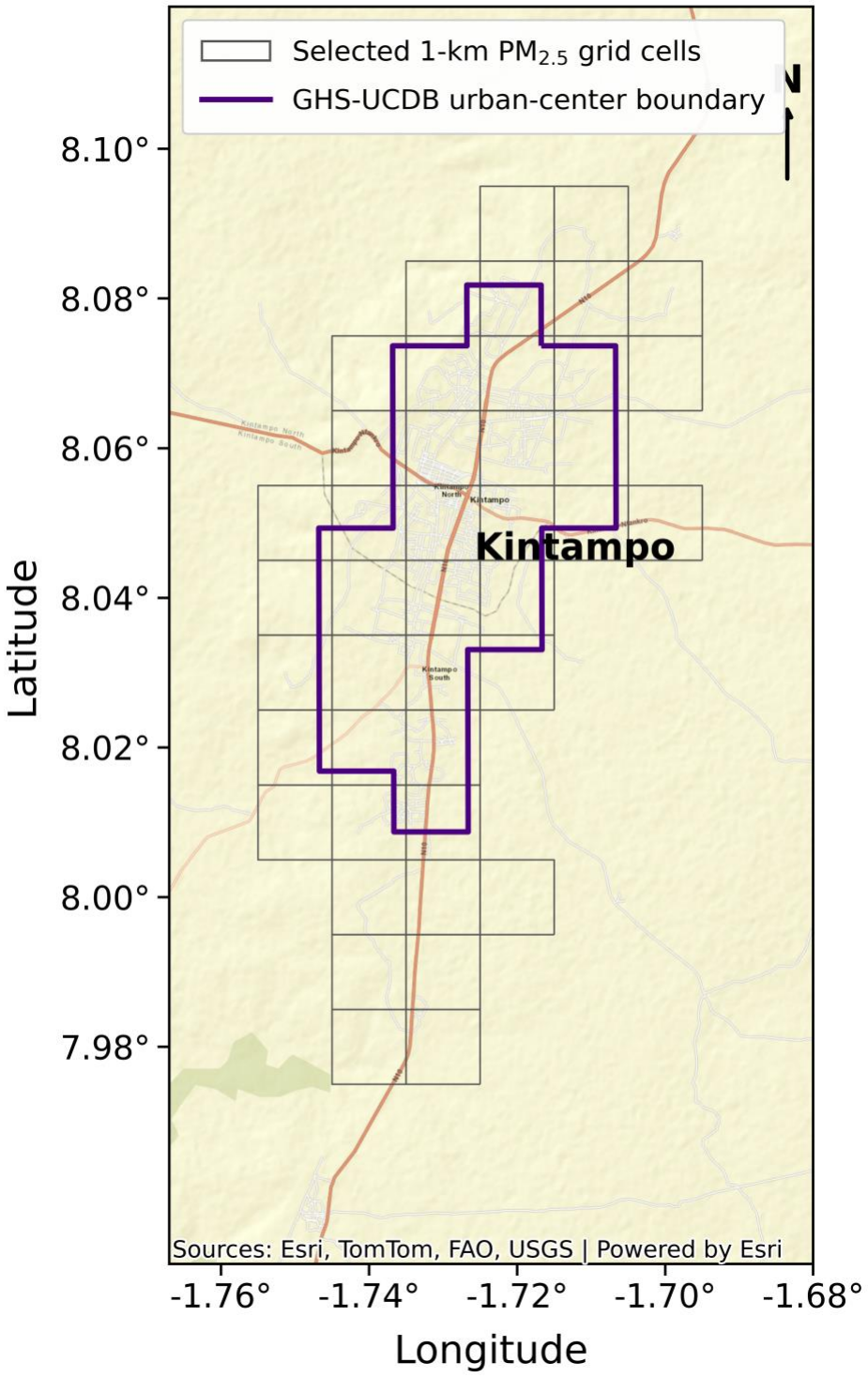


Fig. S7. Spatial selection of $PM_{2.5}$ grid cells for Kintampo. The 1-km $PM_{2.5}$ grids are indicated by the gray grid lines, and the GHS-UCDB urban-center boundary is shown by the thick purple outline.

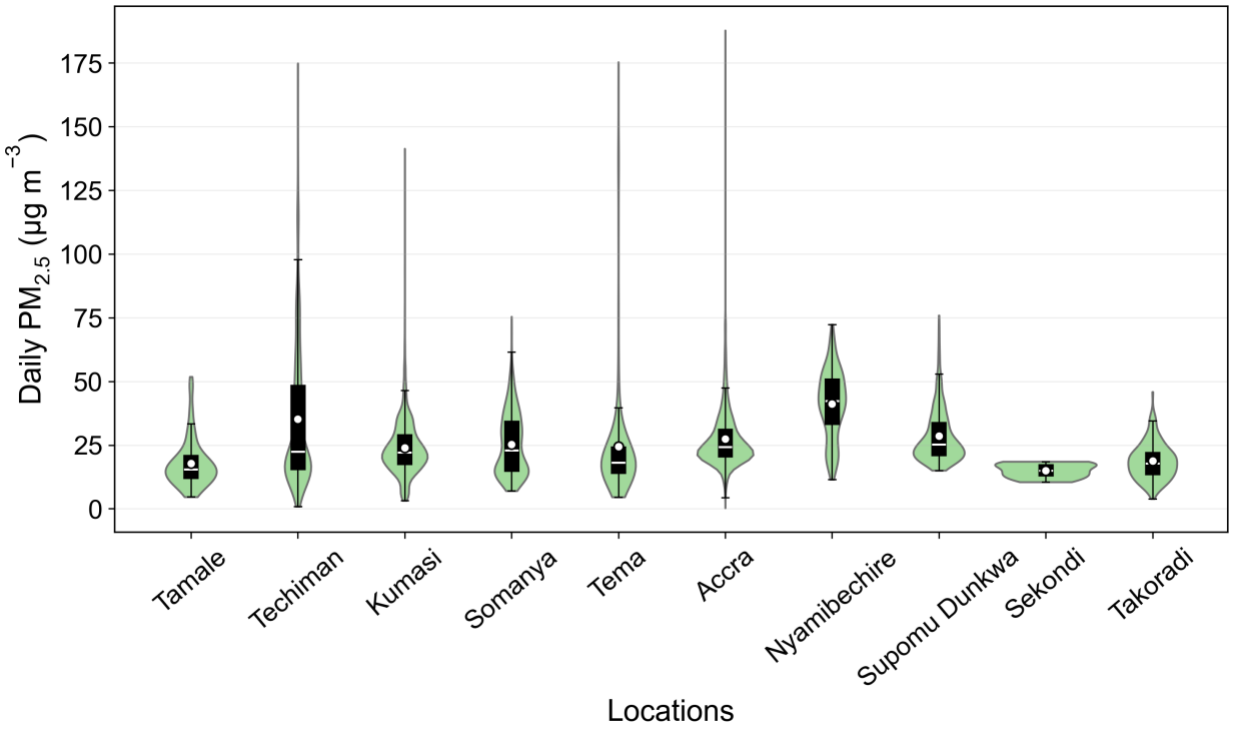


Fig. S8. Violin plots of mean daily $PM_{2.5}$ concentrations measured by ground-based sensors across all study locations in Ghana. Each violin represents the kernel density of daily $PM_{2.5}$ for a location. Embedded boxplots display the median (white horizontal line), mean (white solid circle), and interquartile range (IQR). Whiskers extend to 1.5 × IQR, and values beyond the whiskers are considered outliers.

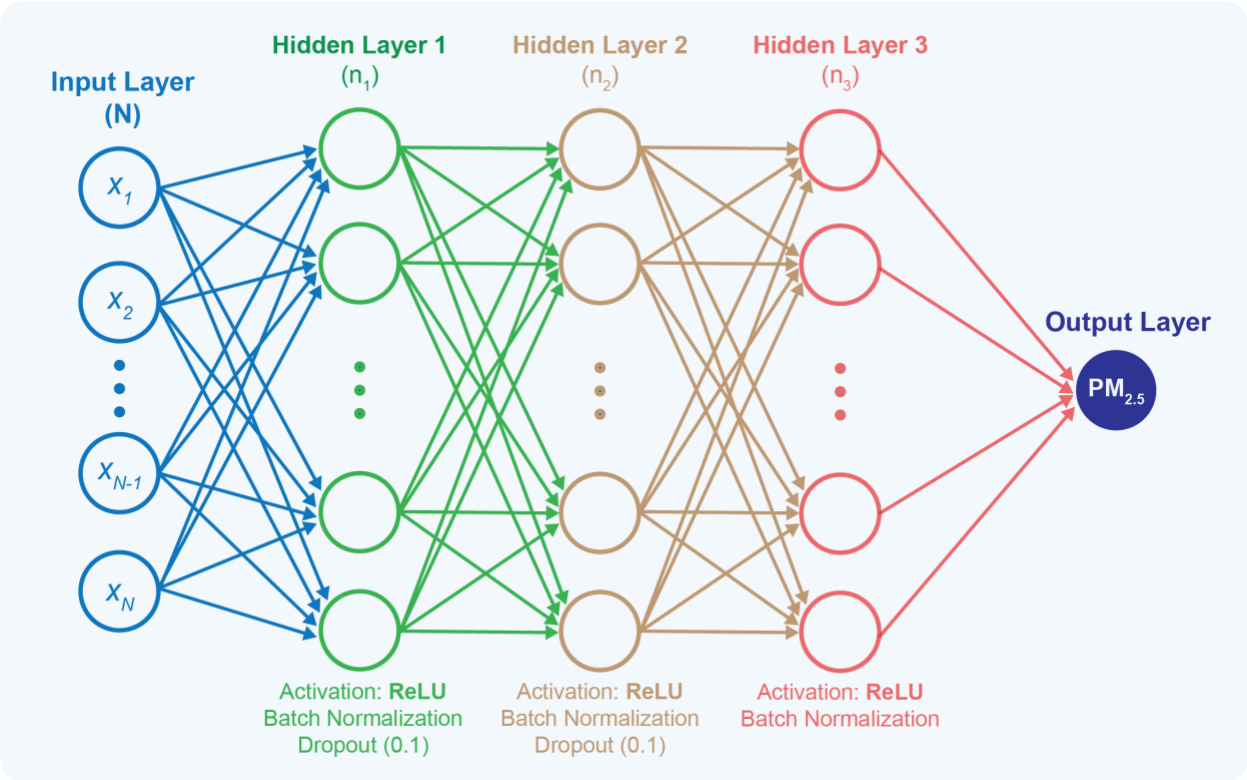


Fig. S9. Architecture of the multilayer perceptron (MLP) model used for $PM_{2.5}$ prediction. The MLP consists of an input layer with N predictor variables (X_1, X_2, ..., X_N). The input layer is followed by three fully connected hidden layers containing n_1, n_2, and n_3 nodes, respectively. Each hidden layer applies a ReLU activation function and batch normalization, while dropout (0.1) is applied to the first two hidden layers to reduce overfitting. The output layer contains a single neuron that produces continuous $PM_{2.5}$ concentrations using a linear activation function. The number of nodes in each hidden layer varies across tested model configurations and is summarized in Tables S5 to S7.

Table S5. Optimized hyperparameters for TROPOMI model. Final tuned hyperparameter values for each machine learning model trained for TROPOMI model of the multi-model framework.

Model	**Optimized hyperparameters**
LASSO	*{'regressor__alpha': 0.01}*
SVM	*{'regressor__C': 100,* *'regressor__epsilon': 0.2,* *'regressor__gamma': 'scale'}*
XGBoost	*{'regressor__learning_rate': 0.1,* *'regressor__max_depth': 7,* *'regressor__n_estimators': 50,* *'regressor__subsample': 1.0}*
RF	*{'regressor__max_depth': 20,* *'regressor__min_samples_split': 5,* *'regressor__n_estimators': 500}*
MLP	*{'layers': [input (N=14) → 256 (n_1) → 128 (n_2) → 64 (n_3) → 1],* *'activation': ReLU,* *'batch_norm': True,* *'dropout': 0.1,* *'optimizer': AdamW,* *'learning_rate': 0.0005,* *'weight_decay': 1e-4,* *'loss': Huber(delta=10),* *'batch_size': 64,* *'epochs': 150}*

Table S6. Optimized hyperparameters for OMI Model. Final tuned hyperparameter values for each machine learning model trained for OMI model of the multi-model framework.

Model	**Optimized hyperparameters**
LASSO	*{'regressor__alpha': 0.01}*
SVM	*{'regressor__C': 100,* *'regressor__epsilon': 0.2,* *'regressor__gamma': 0.1}*
XGBoost	*{'regressor__learning_rate': 0.1,* *'regressor__max_depth': 7,* *'regressor__n_estimators': 50,* *'regressor__subsample': 1.0}*
RF	*{'regressor__max_depth': 20,* *'regressor__min_samples_split': 5,* *'regressor__n_estimators': 500}*
MLP	*{'layers': [input (N=14) → 256 (n_1) → 128 (n_2) → 64 (n_3) → 1],* *'activation': ReLU,* *'batch_norm': True,* *'dropout': 0.1,* *'optimizer': AdamW,* *'learning_rate': 0.0005,* *'weight_decay': 1e-4,* *'loss': Huber(delta=10),* *'batch_size': 64,* *'epochs': 150}*

Table S7. Optimized hyperparameters for MERRA-2 model. Final tuned hyperparameter values for each machine learning model trained for MERRA-2 model of the multi-model framework.

Model	**Optimized hyperparameters**
LASSO	*{'regressor__alpha': 0.001}*
SVM	*{'regressor__C': 100,* *'regressor__epsilon': 0.2,* *'regressor__gamma': 0.1}*
XGBoost	*{'regressor__learning_rate': 0.1,* *'regressor__max_depth': 7,* *'regressor__n_estimators': 50,* *'regressor__subsample': 1.0}*
RF	*{'regressor__max_depth': 20,* *'regressor__min_samples_split': 5,* *'regressor__n_estimators': 500}*
MLP	*{'layers': [input (N=14) → 256 (n_1) → 128 (n_2) → 64 (n_3) → 1],* *'activation': ReLU,* *'batch_norm': True,* *'dropout': 0.1,* *'optimizer': AdamW,* *'learning_rate': 0.0005,* *'weight_decay': 1e-4,* *'loss': Huber(delta=10),* *'batch_size': 64,* *'epochs': 150}*

Table S8. Performance metrics for TROPOMI Model. Performance comparison of machine learning models for $PM_{2.5}$ prediction under random, temporal, and spatial cross-validation schemes. Model performance is evaluated using coefficient of determination (R^2), Pearson correlation (r), bias, root mean squared error (RMSE), and mean absolute error (MAE). Normalized RMSE (nRMSE) and normalized MAE (nMAE) are reported in parentheses. Temporal cross-validation evaluates model generalization across years, while spatial cross-validation assesses transferability across locations. RMSE, MAE and bias are expressed in $\mu g\ m^{-3}$.

Model	Random CV				Temporal CV				Spatial CV			
	R^2 (r)	Bias	RMSE (nRMSE)	MAE (nMAE)	R^2 (r)	Bias	RMSE (nRMSE)	MAE (nMAE)	R^2 (r)	Bias	RMSE (nRMSE)	MAE (nMAE)
LASSO	0.60 (0.78)	-0.17	15.0 (0.48)	9.7 (0.31)	0.56 (0.75)	0.33	15.7 (0.50)	10.3 (0.33)	0.45 (0.68)	2.96	19.8 (0.57)	13.8 (0.39)
SVM	0.69 (0.83)	-1.55	13.2 (0.42)	7.8 (0.25)	0.55 (0.77)	-0.36	15.8 (0.50)	9.8 (0.31)	0.52 (0.75)	-5.91	19.4 (0.55)	13.3 (0.38)
RF	0.71 (0.85)	0.09	12.7 (0.40)	7.6 (0.24)	0.55 (0.77)	0.77	15.9 (0.50)	10.1 (0.32)	0.56 (0.76)	-1.52	18.4 (0.53)	13.1 (0.37)
XGBoost*	0.72 (0.86)	-0.01	12.5 (0.40)	7.3 (0.23)	0.57 (0.78)	0.66	15.6 (0.49)	9.6 (0.30)	0.57 (0.76)	-0.93	17.3 (0.49)	10.4 (0.33)
MLP	0.71 (0.84)	-0.12	12.8 (0.40)	7.8 (0.25)	0.54 (0.76)	-1.56	16.0 (0.51)	10.4 (0.33)	0.42 (0.66)	-2.75	18.7 (0.54)	13.5 (0.38)

Table S9. Performance metrics for OMI Model. Performance comparison of machine learning models for $PM_{2.5}$ prediction under random, temporal, and spatial cross-validation schemes. Model performance is evaluated using coefficient of determination (R^2), Pearson correlation (r), bias, root mean squared error (RMSE), and mean absolute error (MAE). Normalized RMSE (nRMSE) and normalized MAE (nMAE) are reported in parentheses. Temporal cross-validation evaluates model generalization across years, while spatial cross-validation assesses transferability across locations. RMSE, MAE and bias are expressed in $\mu g\ m^{-3}$.

Model	Random CV				Temporal CV				Spatial CV			
	R^2 (r)	Bias	RMSE (nRMSE)	MAE (nMAE)	R^2 (r)	Bias	RMSE (nRMSE)	MAE (nMAE)	R^2 (r)	Bias	RMSE (nRMSE)	MAE (nMAE)
LASSO	0.58 (0.76)	-0.19	15.4 (0.49)	10.2 (0.32)	0.53 (0.73)	0.35	16.3 (0.52)	10.9 (0.35)	0.38 (0.64)	-4.19	21.7 (0.59)	14.1 (0.41)
SVM	0.68 (0.83)	-1.79	13.4 (0.42)	7.8 (0.25)	0.52 (0.75)	-1.31	16.4 (0.52)	10.0 (0.32)	0.48 (0.73)	-5.55	20.2 (0.57)	13.9 (0.40)
RF	0.71 (0.84)	-0.16	13.0 (0.41)	7.9 (0.25)	0.53 (0.75)	1.46	16.3 (0.52)	10.3 (0.33)	0.48 (0.75)	-1.53	19.3 (0.55)	13.6 (0.39)
XGBoost*	0.72 (0.85)	0.04	12.8 (0.41)	7.7 (0.24)	0.56 (0.76)	0.75	15.6 (0.50)	9.6 (0.31)	0.54 (0.75)	-1.01	18.9 (0.54)	13.5 (0.38)
MLP	0.70 (0.83)	-1.19	13.3 (0.42)	8.1 (0.26)	0.50 (0.71)	1.78	16.6 (0.53)	10.6 (0.34)	0.46 (0.70)	-1.83	19.8 (0.57)	15.5 (0.48)

Table S10. Performance metrics for MERRA-2 model. Performance comparison of machine learning models for $PM_{2.5}$ prediction under random, temporal, and spatial cross-validation schemes. Model performance is evaluated using coefficient of determination (R^2), Pearson correlation (r), bias, root mean squared error (RMSE), and mean absolute error (MAE). Normalized RMSE (nRMSE) and normalized MAE (nMAE) are reported in parentheses. Temporal cross-validation evaluates model generalization across years, while spatial cross-validation assesses transferability across locations. RMSE, MAE and bias are expressed in $\mu g\ m^{-3}$.

Model	Random CV				Temporal CV				Spatial CV			
	R^2 (r)	Bias	RMSE (nRMSE)	MAE (nMAE)	R^2 (r)	Bias	RMSE (nRMSE)	MAE (nMAE)	R^2 (r)	Bias	RMSE (nRMSE)	MAE (nMAE)
LASSO	0.63 (0.79)	-0.19	14.5 (0.46)	9.1 (0.29)	0.58 (0.75)	-0.06	15.2 (0.48)	9.6 (0.30)	0.41 (0.67)	-4.63	18.2 (0.57)	12.0 (0.38)
SVM	0.70 (0.83)	-1.68	12.7 (0.41)	7.6 (0.25)	0.55 (0.76)	-1.17	15.9 (0.50)	9.6 (0.30)	0.37 (0.66)	5.60	19.0 (0.60)	11.9 (0.37)
RF	0.71 (0.84)	0.38	12.6 (0.40)	7.5 (0.24)	0.51 (0.75)	1.37	16.6 (0.53)	10.4 (0.33)	0.47 (0.70)	2.16	17.2 (0.54)	10.8 (0.34)
XGBoost*	0.72 (0.85)	-0.18	12.6 (0.40)	7.2 (0.23)	0.59 (0.78)	0.03	15.2 (0.48)	9.2 (0.29)	0.49 (0.73)	0.39	16.8 (0.50)	10.1 (0.32)
MLP	0.70 (0.83)	1.03	12.9 (0.42)	7.8 (0.26)	0.55 (0.74)	1.92	16.0 (0.51)	9.8 (0.31)	0.44 (0.69)	-1.54	18.0 (0.55)	11.2 (0.35)

Table S11. Annual satellite predictor availability and MERRA-2 fallback across Ghana from 2005–2025. Values represent the annual mean percentage of 1-km grid cells where satellite predictors were available and the corresponding percentage requiring MERRA-2 model-based $PM_{2.5}$ estimates.

Year	Satellite availability (%)	MERRA-2 fallback (%)
2005	65.0	35.0
2006	65.4	34.6
2007	63.8	36.2
2008	63.0	37.0
2009	55.2	44.8
2010	51.7	48.3
2011	52.7	47.3
2012	55.5	44.5
2013	57.3	42.7
2014	55.1	44.9
2015	58.0	42.0
2016	54.2	45.8
2017	56.9	43.1
2018	89.5	10.5
2019	99.0	1.0
2020	99.1	0.9
2021	99.2	0.8
2022	99.2	0.8
2023	99.2	0.8
2024	99.0	1.0
2025	99.2	0.8

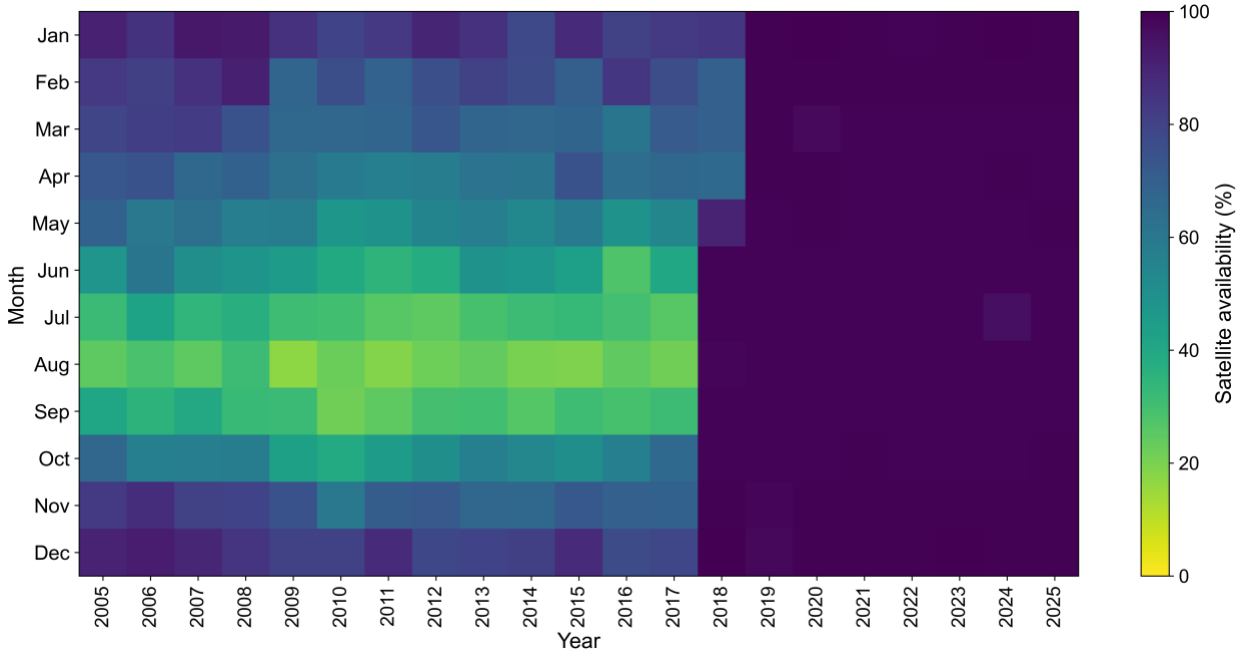


Fig. S10. Monthly satellite predictor availability across Ghana from 2005–2025. Colors indicate the percentage of 1-km grid cells with available satellite predictors for each month and year. Lower satellite availability indicates greater reliance on the MERRA-2 fallback model.

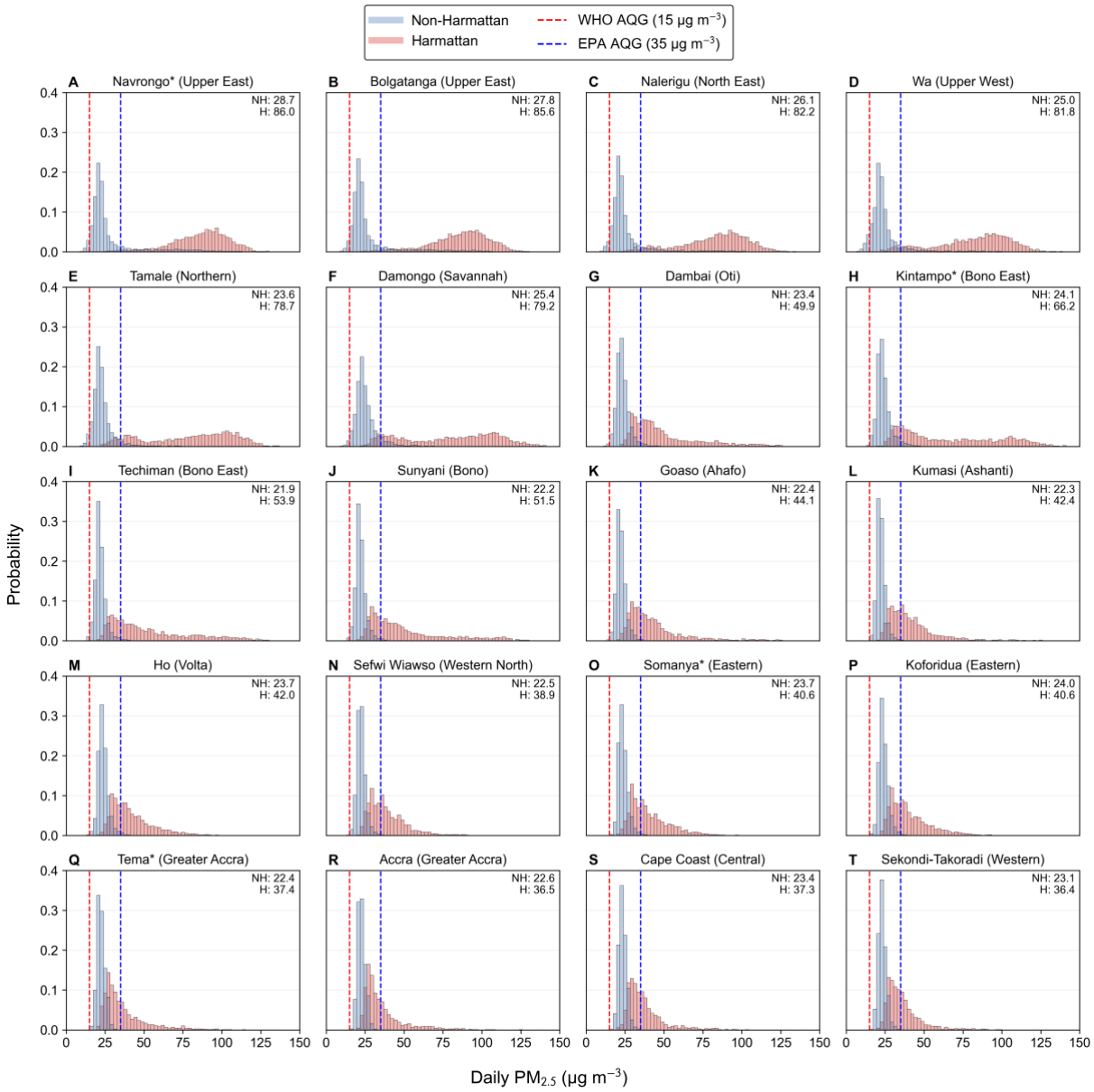


Fig. S11. Distribution of $PM_{2.5}$ concentrations between 2005–2025. (A–T) City-level probability distributions of daily $PM_{2.5}$ concentrations across Ghana during Harmattan and non-Harmattan periods (2005–2025). Panels show histograms of daily mean $PM_{2.5}$ concentrations for each regional capital, arranged geographically from north (top-left) to south (bottom-right). Blue bars represent non-Harmattan conditions, while red bars represent Harmattan conditions (mid-November to mid-March). Average $PM_{2.5}$ (in μg m^{-3}) for both periods are denoted as NH and H for non-Harmattan and Harmattan periods. The red and blue dashed vertical lines indicate the 24-hour air quality guidelines from WHO (15 μg m^{-3}) and Ghana EPA (35 μg m^{-3}), highlighting extremely high number of exceedances, particularly during Harmattan months. Overall, the figure highlights a pronounced north–south gradient in particulate pollution and demonstrates the dominant role of Harmattan dust in shaping seasonal air quality patterns across Ghana.

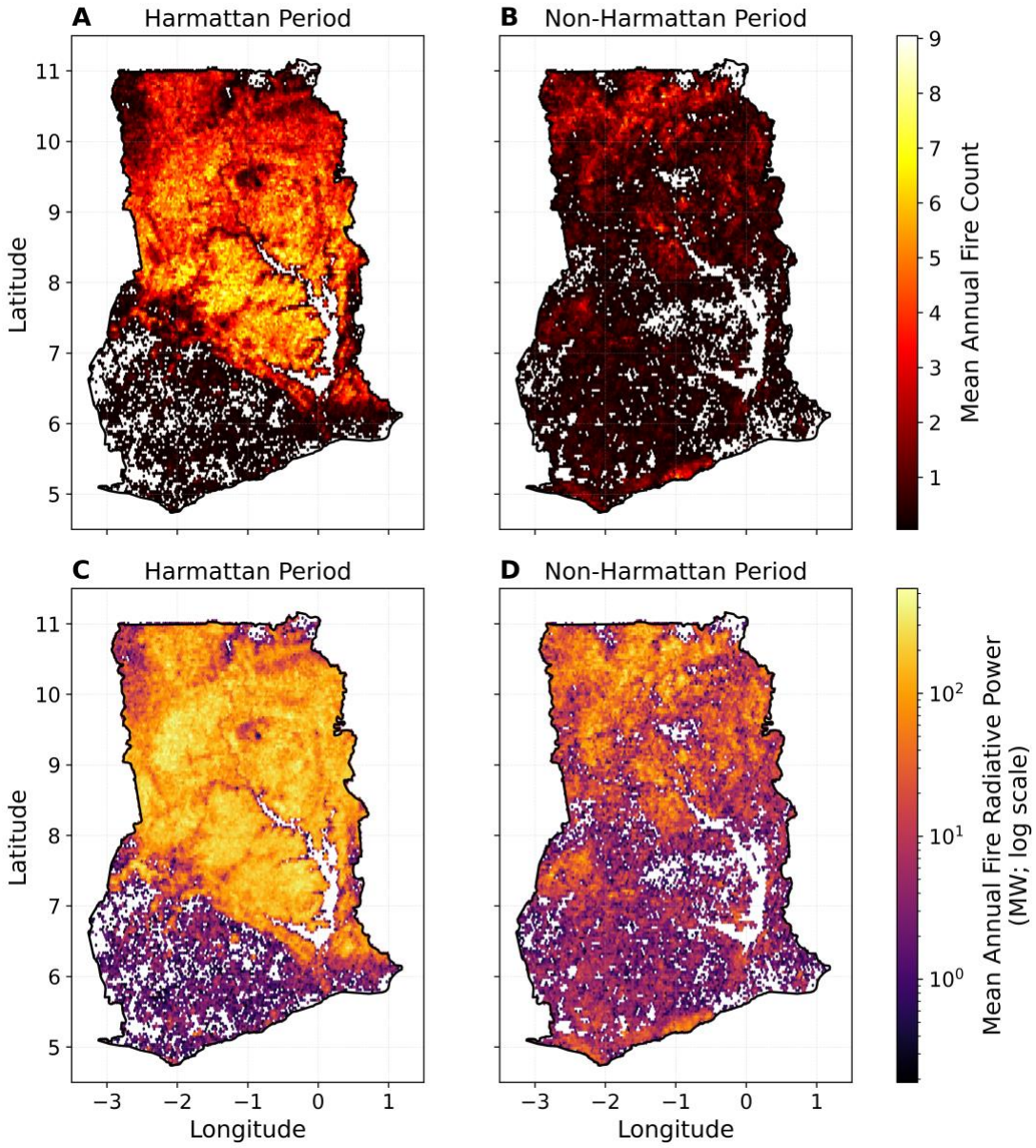


Fig. S12. Spatial distribution of fire activity across Ghana during Harmattan and non-Harmattan seasons (2005–2025). (A–B) Fire detection counts derived from MODIS MCD14ML active fire daily observations aggregated over a 21-year period. (C–D) Corresponding cumulative fire radiative power (FRP), indicating the spatial distribution of fire intensity in megawatts. Harmattan-season fires (December–February; A, C) are concentrated across the northern and middle savanna regions of Ghana, reflecting widespread biomass burning associated with seasonal land management practices and dry atmospheric conditions. In contrast, non-Harmattan fires (March–November; B, D) occur less frequently and are more spatially heterogeneous, with localized hotspots observed across both northern and southern regions. Log-transformed cumulative FRP highlights persistently higher fire intensity across northern Ghana relative to southern forested and coastal zones. All maps include only fire detections with confidence ≥30%.

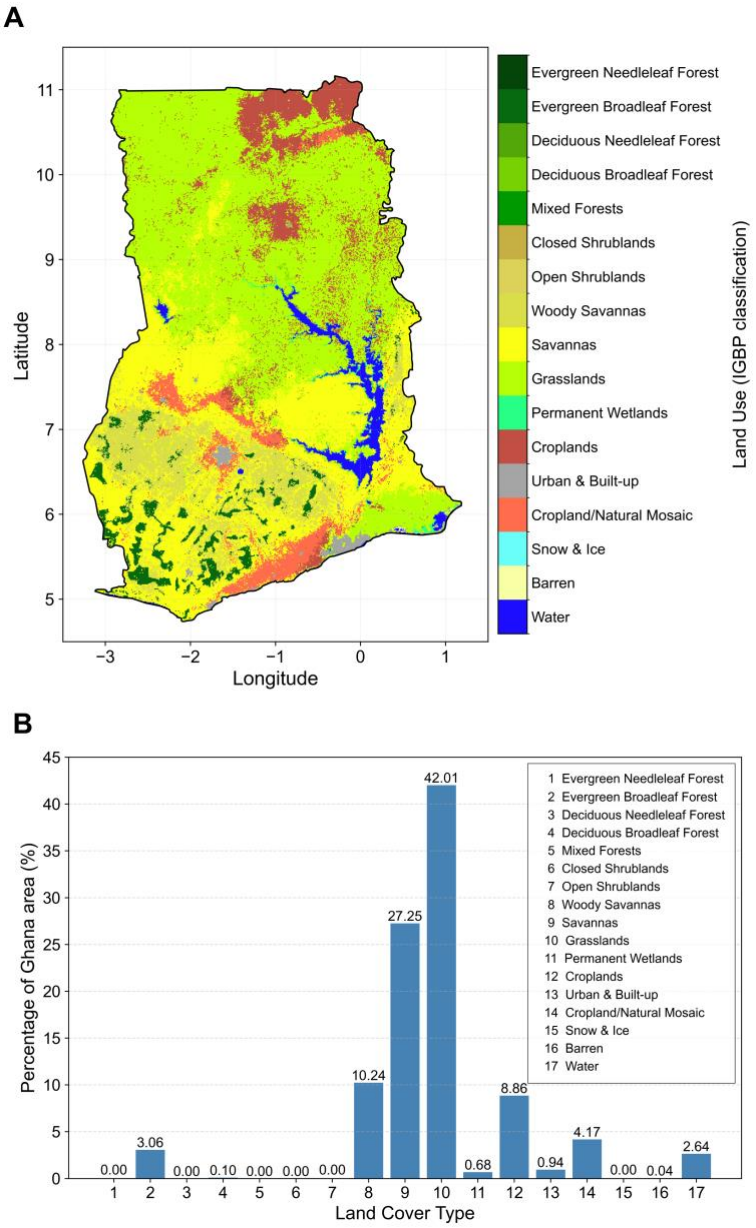


Fig. S13. Land cover distribution across Ghana in 2024. (A) Annual spatial distribution of land cover classes derived from the MCD12Q1 Version 6.1 MODIS Land Cover Type product (International Geosphere–Biosphere Programme, IGBP classification). The original 500 m sinusoidal grid product was regridded to 1 km resolution for Ghana. Savannas and grasslands dominate northern and central Ghana, while croplands and cropland–natural vegetation mosaics are prevalent in southern and transitional zones. Water bodies correspond primarily to Lake Volta and major river systems. (B) Fractional area coverage of each IGBP land cover class within Ghana. Grasslands (42.01%), Savannas (27.25%), woody savannas (10.24%), and croplands (8.86%) represent the dominant land cover types, together accounting for more than 85% of national land area. Only 0.94% of Ghana's land is classified as urban.

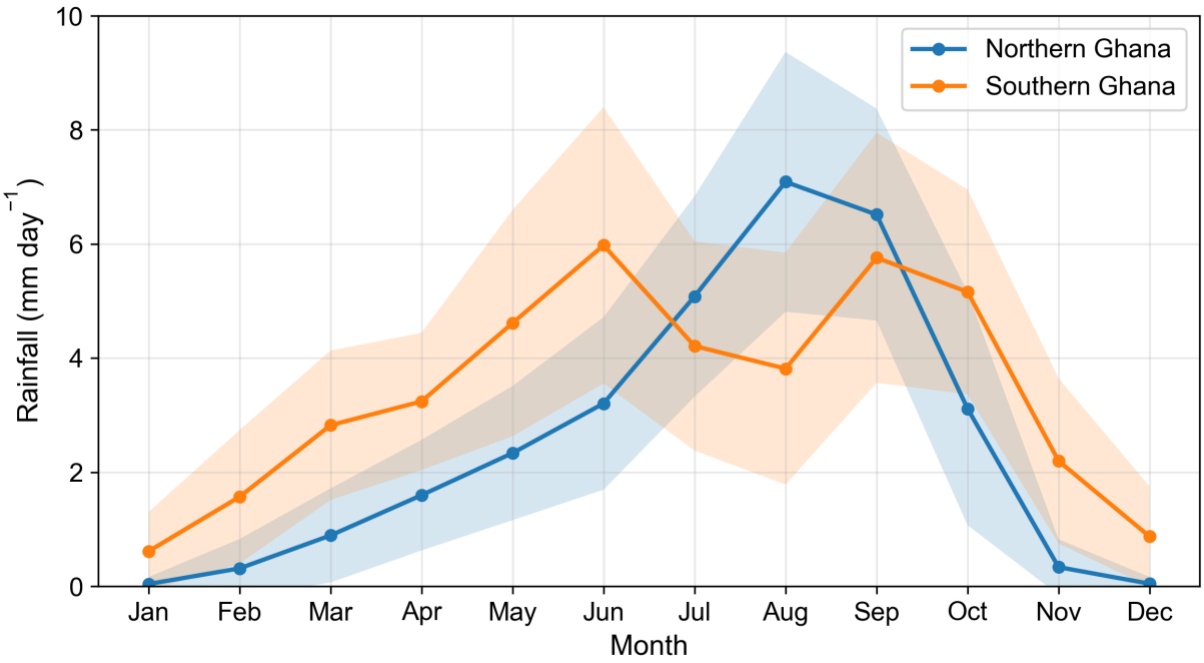


Fig. S14. Monthly rainfall climatology for Northern and Southern Ghana (2005–2025). Lines show the long-term mean daily rainfall for each calendar month derived from ERA5 data, averaged over 2005–2025. Shaded regions represent ±1 standard deviation, indicating interannual variability. Southern Ghana exhibits a bimodal rainfall regime with peaks in May–June (major wet season) and September–October (minor wet season). In contrast, Northern Ghana shows a unimodal rainfall pattern peaking during August–September, a typical characteristic of the West African monsoon.

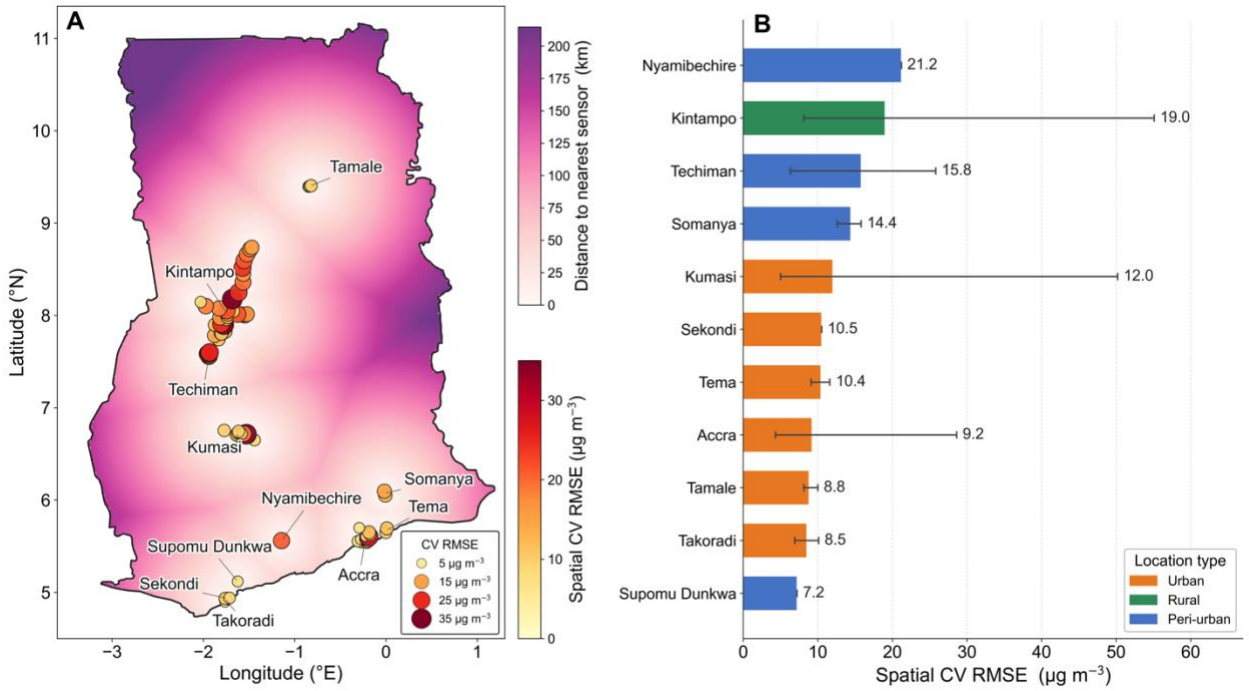


Fig. S15. Spatial uncertainty assessment of the $PM_{2.5}$ model across Ghana. (A) Background color shows the distance to the nearest ground monitoring site, where darker regions indicate areas farther from sensor locations. Circles represent leave-one-site-out cross-validation (CV) RMSE at individual sensor locations, with circle size and color intensity proportional to RMSE magnitude. (B) Mean spatial CV RMSE by city, with horizontal whiskers indicating the full range across monitoring sites within each location. Bar colors denote site classification (urban, peri-urban, and rural). Overall, most monitoring locations exhibit CV RMSE values below 20 µg m^{-3}.

Text S3. Spatial autocorrelation analysis

Global Moran's I was calculated to quantify the degree of spatial autocorrelation in the gridded $PM_{2.5}$ fields. The analysis was performed using a first-order rook neighborhood, in which each grid cell is connected to its immediately adjacent cells in the north, south, east, and west directions. For each year, Global Moran's I was calculated from the spatial $PM_{2.5}$ field using the standardized deviation of each grid cell from the spatial mean and the corresponding values of neighboring cells. The statistic was calculated separately for the 0.01° × 0.01° $PM_{2.5}$ product developed in this study for 2005–2025 and for the Shen et al. (2024) *V6_GL_03* product at 0.01° × 0.01° (fine) and 0.1° × 0.1° (coarse) resolutions for 2005–2024. The Shen et al. (2024) $PM_{2.5}$ product incorporates satellite observations, ground-based measurements, and geophysical a priori information from atmospheric modeling, providing physically based information on the spatial and temporal distribution of $PM_{2.5}$.

Table S12. Comparison of Global Moran's I for the $PM_{2.5}$ product generated in this study and the Shen et al. (2024) $PM_{2.5}$ product at 0.01° × 0.01° and 0.1° × 0.1° resolutions. The mean and range of annual Global Moran's I values are reported for each dataset.

Dataset	**Resolution**	**Years**	**Mean Global Moran's I**	**Range**
This study	0.01° × 0.01°	2005–2025	~0.995	~0.992–0.997
Shen et al. (2024) – *V6_GL_03*	0.01° × 0.01°	2005–2024	0.9985	0.998–0.999
Shen et al. (2024) – *V6_GL_03*	0.1° × 0.1°	2005–2024	0.9885	~0.988–0.989

Text S4. Estimation of long-term $PM_{2.5}$ trends

Long-term trends in $PM_{2.5}$ concentrations were estimated at each grid cell using a non-parametric trend analysis approach applied to the monthly mean $PM_{2.5}$ time series for the period 2005–2025. Monthly mean $PM_{2.5}$ concentrations were calculated from the gridded daily $PM_{2.5}$ dataset for each calendar month. The magnitude of the temporal trend was quantified using Sen's slope estimator, while statistical significance was evaluated using the Seasonal Mann–Kendall (SMK) test, which accounts for recurring seasonal patterns in the time series. Further, the Benjamini–Hochberg false discovery rate (FDR) procedure was applied to account for multiple testing across grid cells.

Mann-Kendall test. The MK test is a rank-based, non-parametric statistical procedure for detecting monotonic trends in time series data (Kendall, 1975; Mann, 1945). The test statistic *S* is computed as:

$$S = \sum_{i=1}^{n-1} \sum_{j=i+1}^{n} \operatorname{sgn}\left(x_j - x_i\right) \ldots \text{(S5)}$$

Where x_i and x_j are observations at times i and j (with $j > i$), n is the total number of observations, and sgn(·) is the sign function returning +1, 0, or −1 for positive, zero, or negative differences, respectively. Under the null hypothesis of no monotonic trend (H_0: the data are independently and identically distributed with no temporal ordering), the standardized test statistic *Z* is given by:

$$Z = \begin{cases} \frac{S-1}{\sqrt{\operatorname{Var}(S)}} & \text{if } S > 0 \\ 0 & \text{if } S = 0 \\ \frac{S+1}{\sqrt{\operatorname{Var}(S)}} & \text{if } S < 0 \end{cases} \ldots \text{(S6)}$$

The variance of *S* is adjusted for tied ranks in the data. A statistically significant positive (negative) *Z* indicates a monotonically increasing (decreasing) trend. We adopt a two-tailed significance threshold of $\alpha = 0.05$, corresponding to $|Z| > 1.96$.

Seasonal Mann-Kendall Test. Monthly means were computed by averaging daily gridded $PM_{2.5}$ concentrations within each calendar month at every 1 km grid cell, yielding a time series of 252 monthly observations per grid cell. Monthly resolution was preferred compared to annual aggregation because it provides substantially more statistical value for trend detection in Ghana while retaining seasonally resolved trend information, such as elevated concentrations during the Harmattan period.

Since $PM_{2.5}$ in Ghana exhibits strong and recurring seasonal cycles, applying the standard MK test directly to the raw monthly time series can conflate underlying long-term trends with seasonal periodicity, inflating or suppressing the apparent trend signal. To address this, we employ the Seasonal Mann-Kendall (SMK) test from Hirsch and Slack (1984), which is specifically designed for time series with seasonal structure. In the SMK framework, the *S* statistic is computed independently for each of the twelve calendar months, comparing, for example, all January values across 2005-2025, all February values across these years, and so on. The resulting within-season statistics are then summed to yield an overall test statistic:

$$S_{\text{total}} = \sum_{g=1}^{12} S_g \ldots \text{(S7)}$$

where S_g is the MK statistic computed for calendar month g. The variance of S_{total} accounts for any covariance between months arising from shared seasonal events (e.g., Harmattan onset), and the final Z statistic is derived from this pooled estimate.

Sen's slope estimator. The magnitude of any statistically significant trend was quantified using Sen's slope estimator, also known as the Theil-Sen estimator (Sen, 1968), which provides a robust, non-parametric measure of the rate of change. Sen's slope β is defined as the median of all pairwise slopes between observations:

$$\beta = \text{median}\left(\frac{x_j - x_i}{j - i}\right), \quad \forall\, j > i \ldots \text{(S8)}$$

where x_i and x_j are the monthly mean $PM_{2.5}$ values for the same calendar month in years i and j. The resulting slope β is expressed in units of μg m^{-3} yr^{-1} and represents the central tendency of the trend rate, resistant to the influence of outliers or single anomalous events such as exceptional dust episodes.

Benjamini–Hochberg false discovery rate (FDR) correction (Benjamini and Hochberg, 1995) was applied to the pixel-wise Seasonal Mann–Kendall p-values to account for multiple statistical testing across the spatial domain. The correction was performed across all valid 1-km grid cells using a false discovery rate threshold of 0.05. The corrected significance criterion was used to identify pixels for which the observed trends remained statistically significant after accounting for multiple comparisons. Pixels with uncorrected $p < 0.05$ that did not satisfy the FDR-adjusted criterion were therefore classified as non-significant. Of the 195,811 valid grid cells, 137,333 (70.14%) had uncorrected $p < 0.05$, compared with 131,061 (66.93%) after FDR correction at $q < 0.05$. Thus, 95.43% of the pixels identified as significant using the uncorrected criterion remained significant after FDR correction.

Table S13. Effect of Benjamini–Hochberg FDR correction on pixel-wise $PM_{2.5}$ trend significance.

Metric	**Uncorrected Seasonal Mann–Kendall**	**Benjamini–Hochberg FDR**
Significance criterion	$p < 0.05$	$q < 0.05$
Valid grid cells tested	195,811	195,811
Statistically significant grid cells	137,333	131,061
Percentage of valid grid cells significant	70.14%	66.93%

Table S14. Annual and seasonal long-term trends in $PM_{2.5}$ concentrations across Ghanaian locations. *Slope* is the Sen's slope estimates ($\mu g\ m^{-3}\ yr^{-1}$), representing the magnitude and direction of monotonic trends derived using monthly $PM_{2.5}$ data (2005–2025). *p–value* is derived from the Seasonal Mann–Kendall (SMK) significance test. Trends with p-values < 0.05 are considered statistically significant and are indicated with an asterisk (*). Non-regional capitals are denoted with a hash (#).

Location	**Annual**		**Harmattan**		**Non-Harmattan**	
	Slope	**p–value**	**Slope**	**p–value**	**Slope**	**p–value**
Navrongo[#]	0.031	0.308	-0.332	0.006*	0.062	0.018*
Bolgatanga	0.024	0.342	-0.285	0.047*	0.044	0.035*
Nalerigu	0.069	0.003*	-0.206	0.228	0.08	<0.001*
Wa	0.108	<0.001*	0	1	0.107	<0.001*
Tamale	0.065	0.001*	0.213	0.264	0.055	0.002*
Damongo	0.054	0.002*	0.416	0.07	0.03	0.055
Dambai	0.008	0.536	0.182	0.054	-0.011	0.37
Kintampo[#]	0.024	0.103	0.31	0.07	0.003	0.896
Techiman	0.049	<0.001*	0.317	0.014*	0.031	0.007*
Sunyani	0.042	0.002*	0.211	0.011*	0.03	0.018*
Goaso	0.012	0.206	0.076	0.217	0.007	0.438
Kumasi	-0.01	0.351	-0.007	0.919	-0.009	0.349
Ho	-0.072	<0.001*	-0.02	0.653	-0.072	<0.001*
Sefwi Wiawso	-0.002	0.896	0.051	0.197	-0.004	0.636
Somanya[#]	-0.086	<0.001*	-0.049	0.264	-0.095	<0.001*
Koforidua	-0.069	<0.001*	0.024	0.591	-0.077	<0.001*
Tema[#]	-0.023	0.006*	-0.032	0.495	-0.023	0.007*
Accra	-0.011	0.2	0.006	0.919	-0.012	0.114
Cape Coast	-0.036	0.001*	-0.064	0.047*	-0.029	0.01*
Sekondi-Takoradi	-0.03	0.001*	-0.065	0.065	-0.022	0.01*

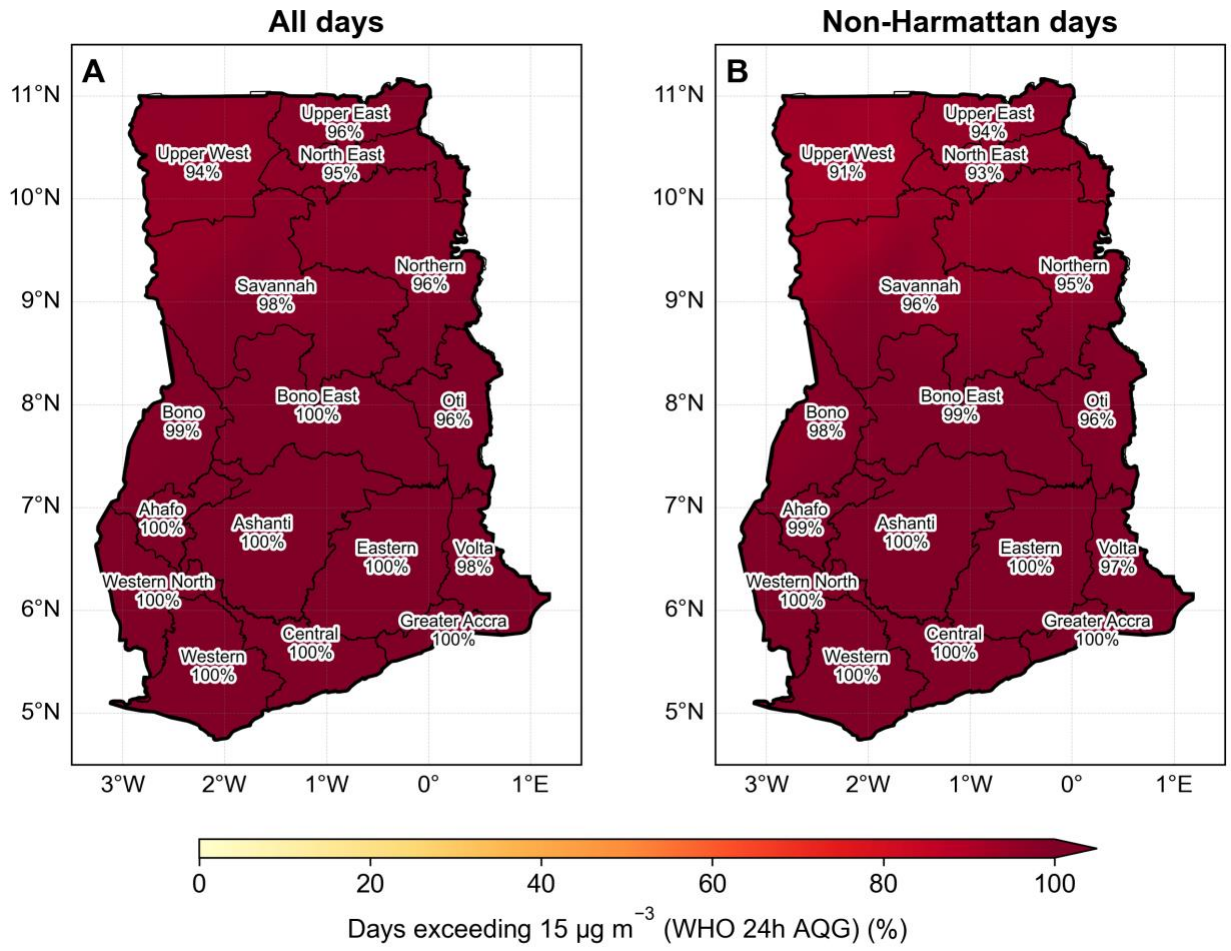


Fig. S16. Spatial distribution of the percentage of days exceeding the WHO 24-hour $PM_{2.5}$ guideline. Maps show the percentage of days during 2005–2025 in which daily $PM_{2.5}$ concentrations exceeded the WHO 24-hour air quality guideline (15 µg m^{-3}) across Ghana, calculated using (a) all available days and (b) non-Harmattan days. Values represent the proportion of days (%) at each grid cell exceeding the guideline threshold.

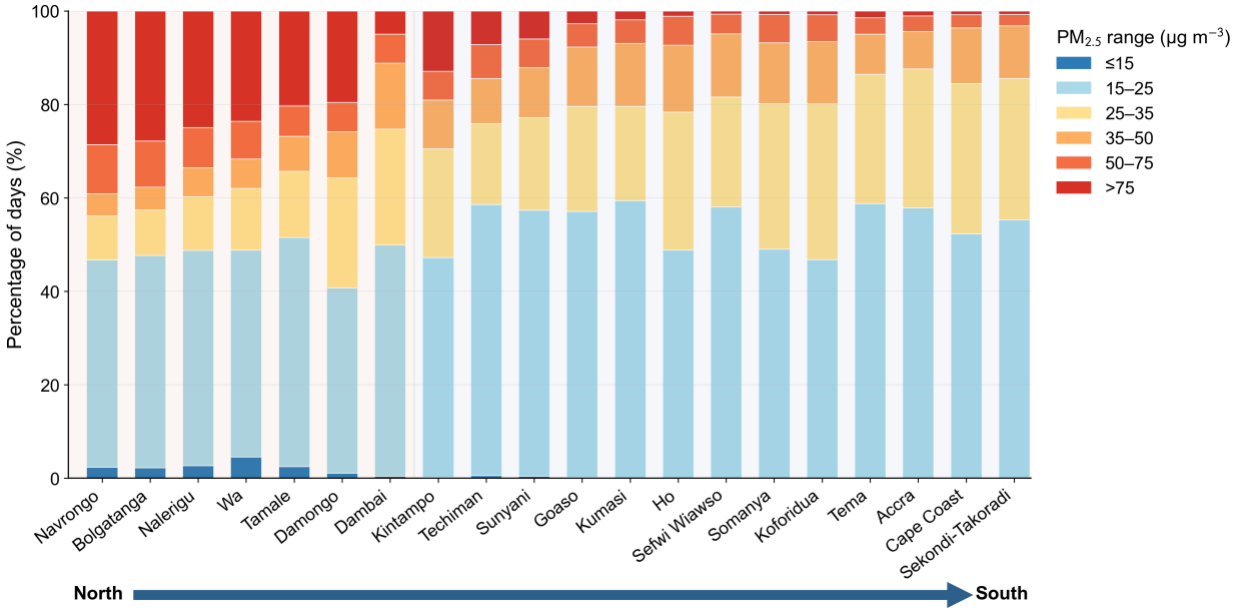


Fig. S17. Distribution of daily $PM_{2.5}$ concentrations across WHO air quality guideline (AQG) categories. Stacked bars show the percentage of days within each concentration range (≤15, 15–25, 25–35, 35–50, 50–75, and >75 µg m^{-3}) for locations across Ghana (2005–2025). Cities are ordered geographically from north (left) to south (right) to highlight spatial gradients in air quality.

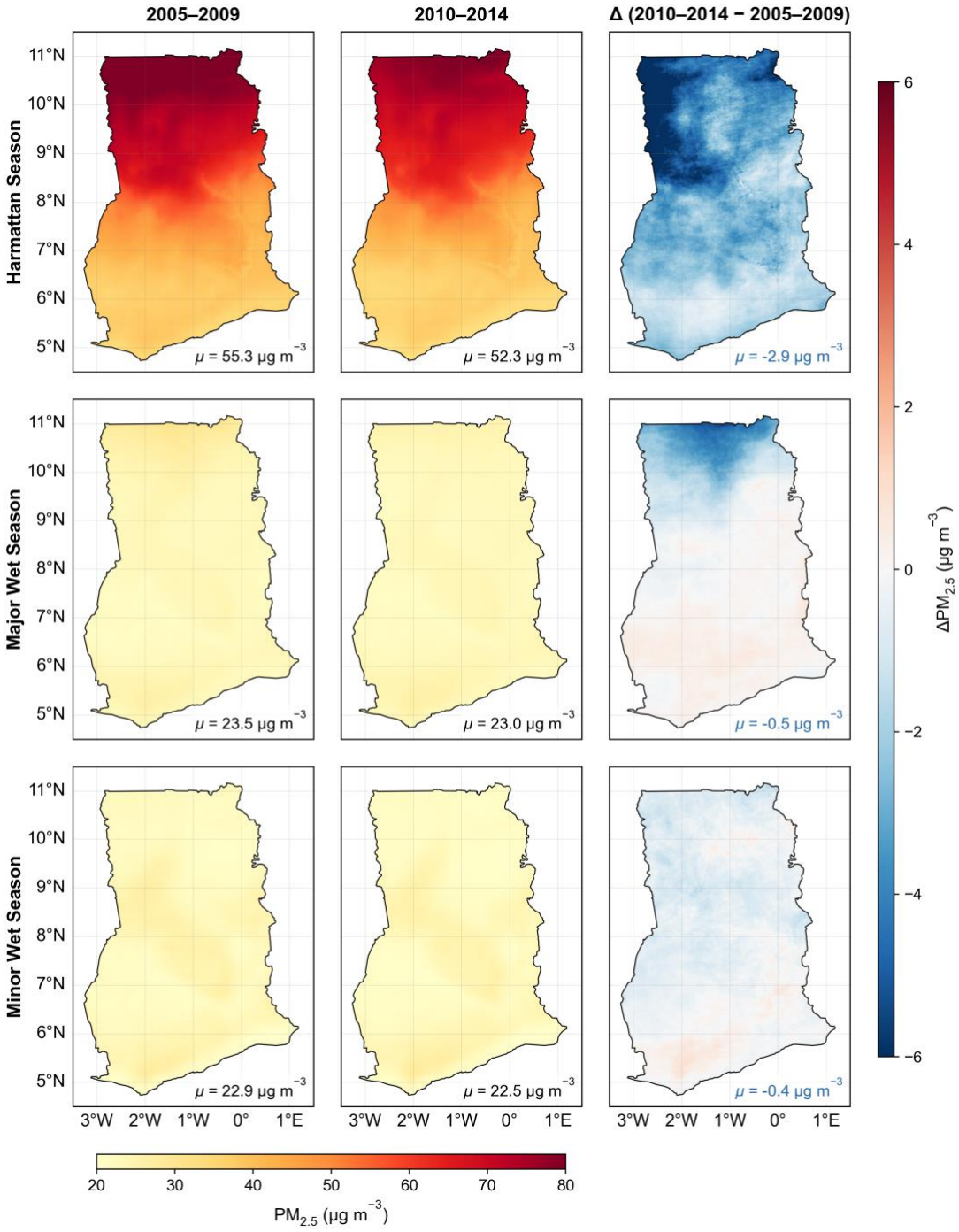


Fig. S18. Multi-year changes in seasonal mean $PM_{2.5}$ concentrations across Ghana (2005–2014). Maps show spatial patterns of mean $PM_{2.5}$ concentrations for the Harmattan, major wet, and minor wet seasons for two multi-year periods (2005–2009 and 2010–2014), along with the corresponding differences (Δ = 2010–2014 minus 2005–2009). μ denotes the spatial mean concentration for each panel. The color scale for mean concentration levels is shown at the bottom, while the diverging color scale on the right indicates the difference.

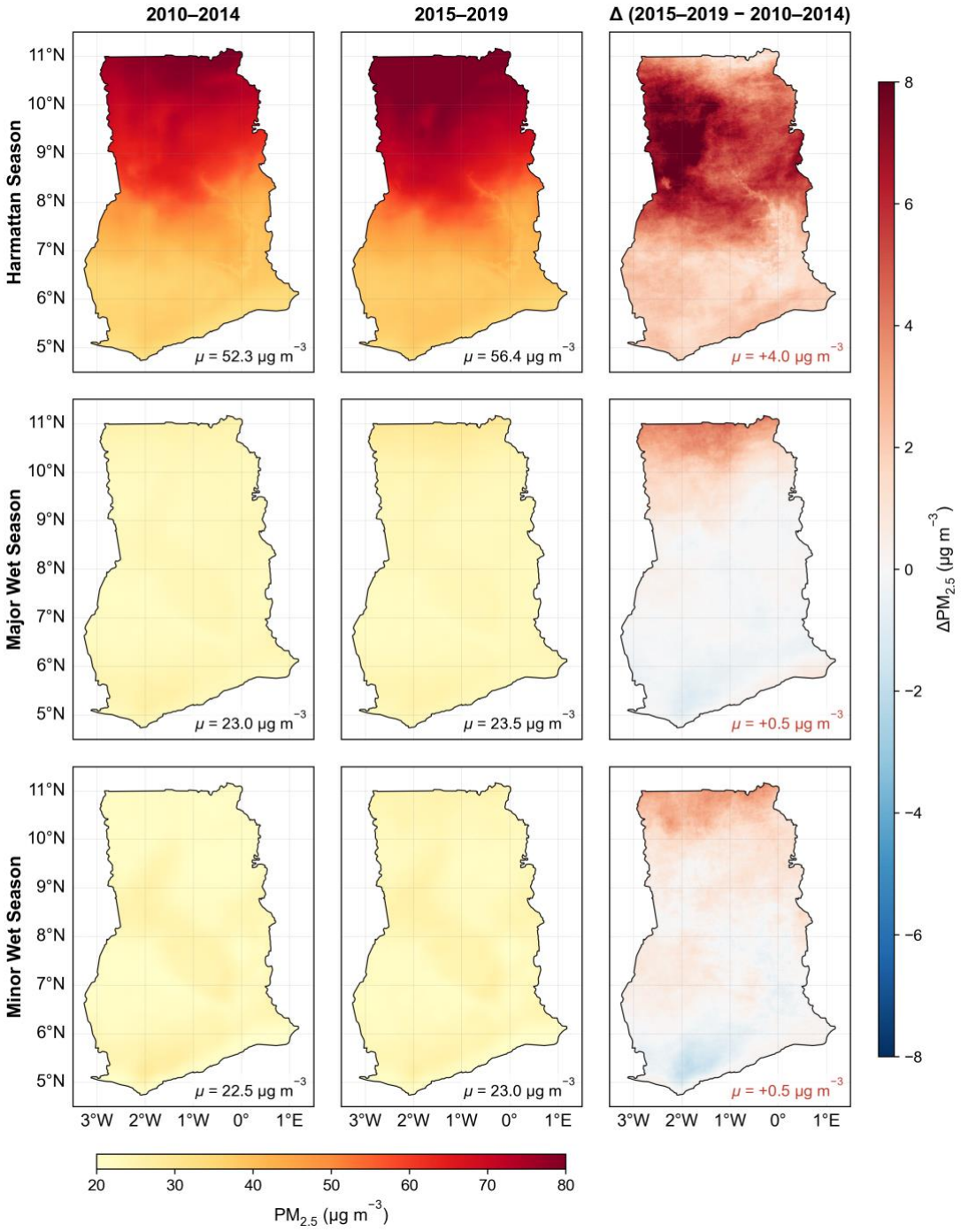


Fig. S19. Multi-year changes in seasonal mean $PM_{2.5}$ concentrations across Ghana (2010–2019). Maps show spatial patterns of mean $PM_{2.5}$ concentrations for the Harmattan, major wet, and minor wet seasons for two multi-year periods (2010–2014 and 2015–2019), along with the corresponding differences (Δ = 2015–2019 minus 2010–2014). μ denotes the spatial mean concentration for each panel. The color scale for mean concentration levels is shown at the bottom, while the diverging color scale on the right indicates the difference.

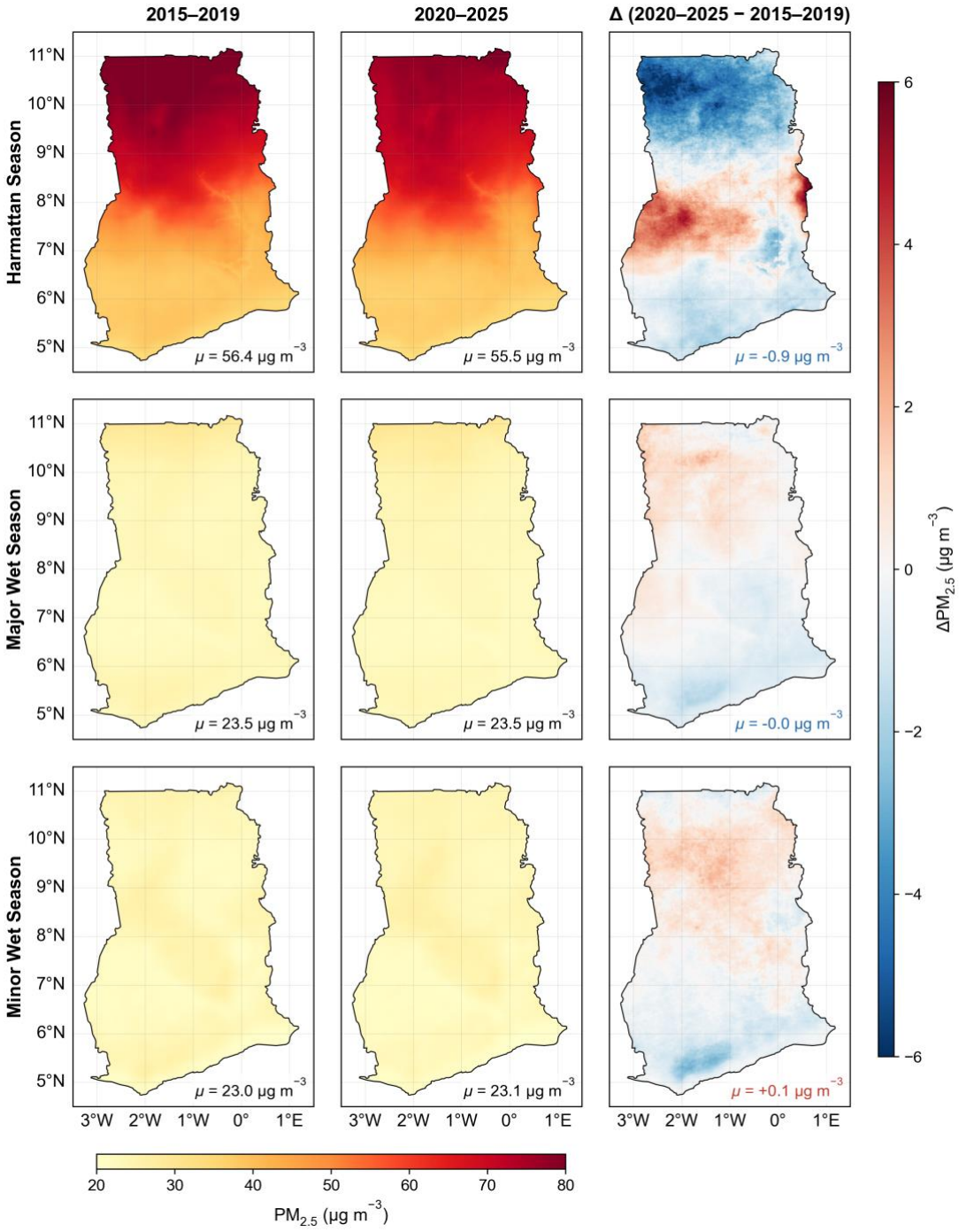


Fig. S20. Multi-year changes in seasonal mean $PM_{2.5}$ concentrations across Ghana (2015–2025). Maps show spatial patterns of mean $PM_{2.5}$ concentrations for the Harmattan, major wet, and minor wet seasons for two multi-year periods (2015–2019 and 2020–2025), along with the corresponding differences (Δ = 2020–2025 minus 2015–2019). μ denotes the spatial mean concentration for each panel. The color scale for mean concentration levels is shown at the bottom, while the diverging color scale on the right indicates the difference.

References

Benjamini, Y. and Hochberg, Y.: Controlling the False Discovery Rate: A Practical and Powerful Approach to Multiple Testing, Journal of the Royal Statistical Society: Series B (Methodological), 57, 289–300, https://doi.org/10.1111/J.2517-6161.1995.TB02031.X, 1995.

Hirsch, R. M. and Slack, J. R.: A Nonparametric Trend Test for Seasonal Data With Serial Dependence, Water Resour. Res., 20, 727–732, https://doi.org/10.1029/WR020I006P00727, 1984.

Kendall, M. G.: Rank Correlation Methods (4th ed.), 1975.

Lebakula, V., Gonzales, J., Stipek, C., Tsybina, E., Zimmer, A., Nukavarapu, N., Jeong, B., Reynolds, B., Kaufman, J., Fan, J., Martin, A., Buck, W., Basford, S., Faxon, A., Meade, S., and Urban, M.: LandScan 2024 [Dataset], Oak Ridge National Laboratory, https://doi.org/10.48690/1532445, 2024.

Mann, H. B.: Nonparametric Tests Against Trend, Econometrica, 13, 245, https://doi.org/10.2307/1907187, 1945.

Melchiorri, M., Mari, R. I., Florio, P., Schiavina, M., Krasnodebska, K., Politis, P., Uhl, J., Pesaresi, M., Maffenini, L., Sulis, P., Crippa, M., Guizzardi, D., Pisoni, E., Belis, C., Oom, D., Branco, A., Mwaniki, D., Githira, D., Kochulem, E., Tommasi, P., Carioli, A., Ehrlich, D., Kemper, T., and Dijkstra, L.: Stats in the City – the GHSL Urban Centre Database 2025, European Commission, Joint Research Centre (JRC), https://doi.org/10.2760/3046391, 2024.

Owusu-Tawiah, V., Annor, T., Yamba, E. I., Nimo, J., Wemegah, C. S., Hodoli, C. G., Osei-Tutu, D., Amponsah, D., Hughes, A. F., and Westervelt, D. M.: Spatiotemporal Assessment of PM2.5 in Senior High Schools in Kumasi, Ghana using Low-Cost Sensors, Aerosol Air Qual. Res., 25, 66-, https://doi.org/10.1007/S44408-025-00066-2, 2025.

Raheja, G., Nimo, J., Appoh, E. K. E., Essien, B., Sunu, M., Nyante, J., Amegah, M., Quansah, R., Arku, R. E., Penn, S. L., Giordano, M. R., Zheng, Z., Jack, D., Chillrud, S., Amegah, K., Subramanian, R., Pinder, R., Appah-Sampong, E., Tetteh, E. N., Borketey, M. A., Hughes, A. F., and Westervelt, D. M.: Low-Cost Sensor Performance Intercomparison, Correction Factor Development, and 2+ Years of Ambient PM2.5 Monitoring in Accra, Ghana, Environ. Sci. Technol., 57, 10708–10720, https://doi.org/10.1021/ACS.EST.2C09264, 2023.

Sen, P. K.: Estimates of the Regression Coefficient Based on Kendall's Tau, J. Am. Stat. Assoc., 63, 1379–1389, https://doi.org/10.1080/01621459.1968.10480934, 1968.

Shen, S., Li, C., van Donkelaar, A., Jacobs, N., Wang, C., and Martin, R. V.: Enhancing Global Estimation of Fine Particulate Matter Concentrations by Including Geophysical a Priori Information in Deep Learning, ACS ES&T Air, 1, 332–345, https://doi.org/10.1021/ACSESTAIR.3C00054, 2024.